

MedAugment: Universal Automatic Data Augmentation Plug-in for Medical Image Analysis

Zhaoshan Liu^{a,*}, Qiuji Lv^{a,b,*}, Yifan Li^a, Ziduo Yang^{a,b}, Lei Shen^{a,**}

^a*Department of Mechanical Engineering, National University of Singapore, 9 Engineering Drive 1, Singapore, 117575, Singapore*

^b*School of Intelligent Systems Engineering, Sun Yat-sen University, No.66, Gongchang Road, Guangming District, 518107, China*

Abstract

Data augmentation (DA) has been widely leveraged in the realm of computer vision to alleviate the data shortage, whereas the DA in medical image analysis (MIA) faces multiple challenges. The prevalent DA approaches in MIA encompass conventional DA, synthetic DA, and automatic DA. However, the utilization of these approaches poses various challenges such as experience-driven design and intensive computation cost. Here, we propose an efficient and effective automatic DA method termed MedAugment. We propose the pixel augmentation space and spatial augmentation space and exclude the operations that can break the details and features within medical images. Besides, we propose a novel sampling strategy by sampling a limited number of operations from the two spaces. Moreover, we present a hyperparameter mapping relationship to produce a rational augmentation level and make the MedAugment fully controllable using a single hyperparameter. These revisions address the differences between natural and medical images. Extensive experimental results on four classification and three segmentation datasets demonstrate the superiority of MedAugment. We posit that the plug-and-use and training-free MedAugment holds the potential to make a valuable contribution to the medical field, particularly benefiting medical experts lacking foundational expertise in deep learning. Code is available at <https://github.com/NUS-Tim/MedAugment>.

Keywords: Data Augmentation, Medical Image Analysis, Image Classification, Image Segmentation

*Equal contribution

**Corresponding author

Email addresses: e0575844@u.nus.edu (Zhaoshan Liu), lvqj5@mail2.sysu.edu.cn (Qiuji Lv), e0576095@u.nus.edu (Yifan Li), yangzd@mail2.sysu.edu.cn (Ziduo Yang), mpeshel@nus.edu.sg (Lei Shen)

1. Introduction

Medical image analysis (MIA) employs various imaging modalities to create a visual representation of the interior body and assist with further medical diagnoses. Currently, MIA is predominantly conducted by medical experts and this time-consuming and labor-intensive process can potentially result in variability in interpretation and accuracy. To this end, deep learning (DL) has been adopted into the MIA field to assist MIA, especially for the mainstream classification and segmentation tasks. Though DL-based MIA has achieved promising results [1–4], ensuring the performance of the DL model under data scarcity can be challenging. Differing from natural images [5], the scarcity of data in MIA can be attributed to two primary factors. Firstly, collecting medical images necessitates specialized equipment and requires expert annotation. Secondly, the distribution of collected images is constrained by patient privacy concerns [6]. In this context, various techniques have been proposed to mitigate the data shortage, and data augmentation (DA) is the most prevalent and effective one [7]. The DA improves the performance and generalization capability of the model by enhancing the diversity and richness of data, and its prevalent usage in the realm of MIA includes conventional DA, synthetic DA, and automatic DA.

The conventional DA method leverages various DA operations such as rotation, flip, and translation [7] to compose varying DA pipelines. This approach, while straightforward and effective in MIA [8–12], presents distinct challenges. The pipeline design such as operation selection, sequence adjustment, and magnitude determination heavily relies on experience. This may not be suitable for personnel without a solid DL foundation and can lead to suboptimal augmentation diversity. Leveraging generative adversarial network (GAN) [13] to perform DA is one of the most prevalent synthetic methods. The GAN encompasses the generator and discriminator playing an adversarial game, in which the generator learns to synthesize realistic artificial images and the discriminator strives to distinguish real and synthesized images. However, the utilization of GAN in MIA [14–23] faces various challenges, including time-consuming and data-hungry training [24, 25] and varying synthesized quality. Except for leveraging GAN, several researchers utilize the diffusion model [26] to augment medical images [27–30]. However, this approach faces low sampling speed and high computational cost [29].

The automatic DA [31–36] consists of an augmentation space with various conventional operations, and the input is augmented through the operations sampled from the space. This can produce varying augmentations for input thus enhancing data diversity and model generalization ability. Though various automatic DA approaches [31–40] have been adapted for MIA, these approaches can be unsuitable for medical images and computationally extensive. The ubiquitous data shortage [20, 41, 42], together with the augmentation challenges encountered, hampers the model performance in MIA to a large extent. To address the data shortage and challenges confronted, we propose an efficient and effective automatic DA method MedAugment. In contrast to the existing methods with single augmentation space,

we present two augmentation spaces termed pixel augmentation space A_p and spatial augmentation space A_s and exclude the operations that can disrupt the details and features in medical images. Besides, we propose a novel operation sampling strategy by constraining the number of operations sampled from the two spaces. Moreover, we present a hyperparameter mapping relationship to produce a rational augmentation level and make the MedAugment fully controllable with a single hyperparameter. These modifications effectively tackle the differences between natural and medical images. Extensive experimental results on four classification and three segmentation datasets demonstrate the leadership of the proposed MedAugment. The plug-and-use and training-free MedAugment may benefit the MIA community, especially medical experts without solid DL foundations. To sum up, our main contributions are:

- We propose an efficient and effective automatic data augmentation method termed MedAugment. The MedAugment is plug-and-use and training-free and performs both medical image classification and segmentation tasks.
- We present pixel augmentation space and spatial augmentation space, along with the novel sampling strategy and hyperparameter mapping relationship to effectively tackle the differences between natural and medical images.
- We perform extensive experiments on four classification and three segmentation datasets and the results demonstrate the superiority of the proposed MedAugment.

The rest of this paper is organized as follows. Section 2 "Related Work" illustrates the recent progress of automatic DA and DA in MIA. Section 3 "Methods" discusses the detailed methodology of the proposed MedAugment. Section 4 "Experiments and Results" demonstrates the datasets, experimental setup, and main results. Detailed analysis and ablation experiments are also conducted. We summarize our work and point out the future perspectives in Section 5 "Conclusions".

2. Related Work

2.1. Automatic Data Augmentation

Numerous automatic DA methods have been developed to combine conventional operations for model performance improvement. In 2019, Cubuk et al. [31] developed an AutoAugment where a policy in search space is composed of several sub-policies and each sub-policy is randomly selected for each image. Each sub-policy consists of two DA operations selected from sixteen. Though AutoAugment achieves promising performance, the DA policy is searched using the reinforcement learning method and thus can be computationally expensive. To this end, Lim and colleagues [32] proposed the Fast AutoAugment to identify the augmentation policy by employing density matching across paired training datasets. The Fast AutoAugment is based on Bayesian DA [43] and can recover additional missing data points

through Bayesian optimization during the policy search phase. Besides, Ho et al. [33] presented a population-based augmentation approach to produce the nonstationary policy rather than the fixed one. These approaches, though reduce the search cost, do not eliminate the separate search phase. Accordingly, Cubuk and colleagues developed a RandAugment [34] method, in which multiple DA operations with the same augmentation level are sequentially leveraged. The augmentation space of RandAugment comprises fourteen operations. Comparable work of RandAugment includes the TrivialAugment [35] that utilizes a single operation and samples the augmentation level anew for each image. Additionally, the UniformAugment [36] fixes the number of operations to two and drops each operation with a probability $p = 0.5$. Besides leveraging DA operations successively, an alternative is to combine them in parallel. For instance, the AugMix [44] randomly samples various operations from nine to compose an augmentation chain. Several augmentation chains and a separate chain without DA are then mixed to derive the augmented images and the weight assigned to each augmented branch is controlled with w . Though these approaches are effective and low-computation, their usage poses various challenges in the realm of MIA. Firstly, the involved operations such as `invert`, `equalize`, and `solarize` can disrupt the intricate details and features characteristic within medical images. Secondly, the sampling strategy tends to overlook the fact that medical images exhibit heightened sensitivity to operations such as `brightness`, `contrast`, and `posterize`. Finally, operations including `brightness` and `contrast` can compromise the grey-level class information stored in the masks, thereby constraining the model performance for image segmentation.

2.2. Data Augmentation in MIA

Most researchers employ the DA approach in MIA [7] and the prevalent utilized methods are threefold. Firstly, most of the studies leverage the conventional DA. For example, Kaushik et al. [11] utilized translation, rotation, scale, flip, etc. to augment fundus images for diabetic retinopathy diagnosis. Khened and colleagues [10] augmented the dataset using rotation, translation, scale, gaussian noise, etc. for cardiac segmentation. Besides, the nnU-Net [12] developed by Isensee et al. leverages a preset DA pipeline consisting of varying operations including rotation, scaling, Gaussian noise, Gaussian blur, etc. in sequence. While the conventional DA method is straightforward and effective, the pipeline design heavily relies on experience and may lead to suboptimal augmentation diversity. Secondly, a large proportion of researchers employ synthetic models such as GAN to synthesize artificial images. For instance, Beers and colleagues [22] proved the feasibility of leveraging PGGAN [45] to synthesize fundus and glioma images. Calimeri et al. [46] employed LAPGAN [46] to generate brain magnetic resonance imaging images. Besides, the DPGAN [14] developed in 2022 consists of three variational auto-encoder GANs to synthesize artificial images and labels. The leveraging of GAN-based approaches raises varying challenges such as time-consuming and data-hungry training and varying synthesize quality. Several studies have concentrated on employing diffusion models to per-

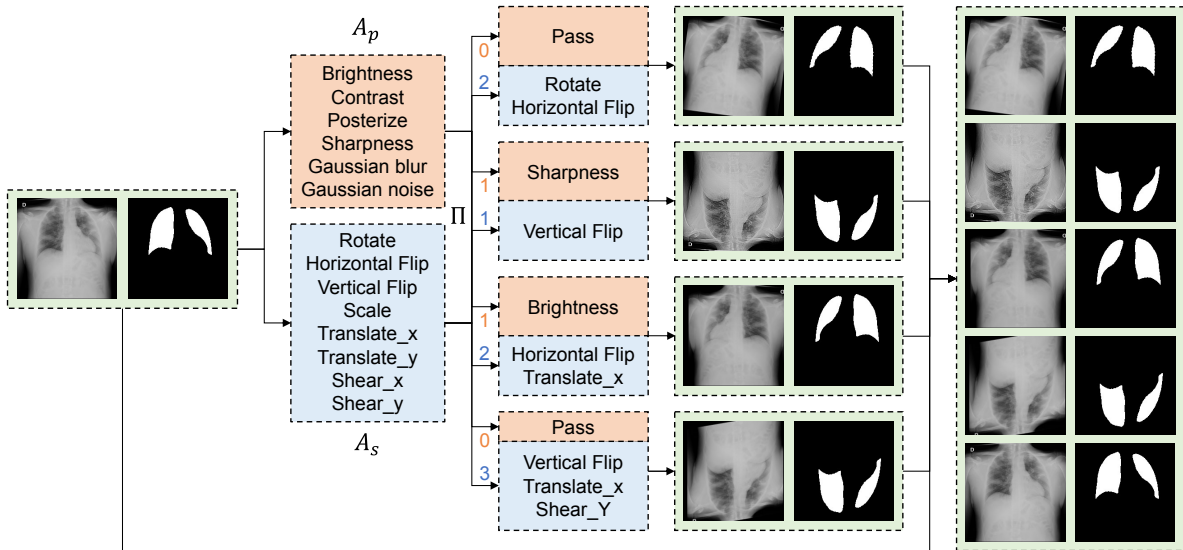


Figure 1: A realization of MedAugment. The MedAugment consists of $N = 4$ augment branches and a separate branch to retain the input features. For each branch, $M = \{2, 3\}$ DA operations are sampled using the sampling strategy Π from the pixel augmentation space A_p and spatial augmentation space A_s .

form synthetic DA as an alternative. For example, Moghadam et al. [27] generated histopathology images by employing diffusion models together with color normalization and prioritized morphology weighting. Pinaya and colleagues [28] leveraged latent diffusion models [47] to synthesize three-dimensional artificial brain images. Additionally, the MGCC developed in 2023 [30] utilizes the images generated by latent diffusion models [47] as unlabeled data when performing semi-supervised segmentation. However, such methods can be constrained by low sampling speed and high computational cost. Thirdly, a group of researchers utilizes the automatic DA approach. For instance, Qin et al. [37] developed a joint-learning strategy to combine segmentation modules and Dueling DQN [48] to search for maximum performance improvement. Xu and colleagues [38] proposed a differentiable way to update the parameters using stochastic relaxation and the Monte Carlo method. The AADG framework [39] developed in 2022 consists of a new proxy task to maximize the diversity among various augmented domains using Sinkhorn distance. Additionally, Yang et al. [40] utilized the validation accuracy to update the controller of the recurrent neural network. These approaches face challenges in computation cost.

3. Methods

3.1. MedAugment

We illustrate a realization of the proposed MedAugment in Figure 1. The MedAugment encompasses $N = 4$ augment branches and a separate branch to retain the input features. We design two augmentation spaces A_p and A_s and exclude the

Algorithm 1 Pseudocode for MedAugment.

Require: Pixel augmentation space $A_p = \{\text{brightness}, \dots, \text{gaussian noise}\}$, Spatial augmentation space $A_s = \{\text{rotate}, \dots, \text{shear_y}\}$, Branch $B = \{b_1, \dots, b_4\}$, Number of sequential operations $M = \{2, 3\}$, Sampling strategy $\Pi = \{\pi_1, \dots, \pi_4\}$, Augmentation level $l = 5$, Max operation magnitude $M_{A_p} = \{0.1l, \dots, -\}$, $M_{A_s} = \{4l, \dots, (0, 0.02l)\}$, Operation probability $P_A = 0.2l$, Input dataset $D = (X, Y)$;

Ensure: Augmented dataset D^a , Output dataset D^o ;

```
1: for all  $X_i, Y_i$  do
2:   for all  $b_j$  do
3:     Sample  $\pi$  from  $\Pi$  without replacement           ▷ strategy-level random
4:     Sample  $M$  operations  $\mathcal{O}_j = \{o_1, \dots, o_m\}$  using  $\pi$  from  $A$ ;
5:     Shuffle  $\mathcal{O}_j$                                      ▷ operation-level random
6:     for all  $o$  do
7:       Calculate  $M_A, P_A$  using  $l$ 
8:       Uniformly sample magnitude  $m \in M_A$          ▷ magnitude-level random
9:     end for
10:     $(X_i^j, Y_i^j) = \mathcal{O}_j(X_i, Y_i)$ 
11:    Add  $(X_i^j, Y_i^j)$  to  $D^a$ 
12:  end for
13: end for
14: Out  $D^o = D^a + D$ 
```

operations that can disrupt the details and features within medical images. The A_p and A_s encompass six and eight DA operations, respectively. Besides, we develop an operation sampling strategy Π to restrict the number of operations sampled from the two spaces, resulting in $M = \{2, 3\}$ sequential DA operations in each augment branch. Moreover, we propose a novel mapping relationship to produce a rational augmentation level and affirm that the maximum magnitude and probability of each operation is controllable with the single augmentation level $l = 5$. These revisions can effectively handle the differences between natural and medical images. It is worth pointing out that some of the operations such as Horizontal flip do not possess magnitude. To sum up, MedAugment introduces randomness from three aspects, including the strategy level, operation level, and magnitude level. For each input image, MedAugment samples the operations for each branch with the sampling strategy. The sampled operations are then shuffled. Finally, the input image is augmented with the shuffled operations, in which the operation magnitude is uniformly sampled within the maximum magnitude and the probability is determined based on l . The pseudo-code of the proposed MedAugment is illustrated in Algorithm 1.

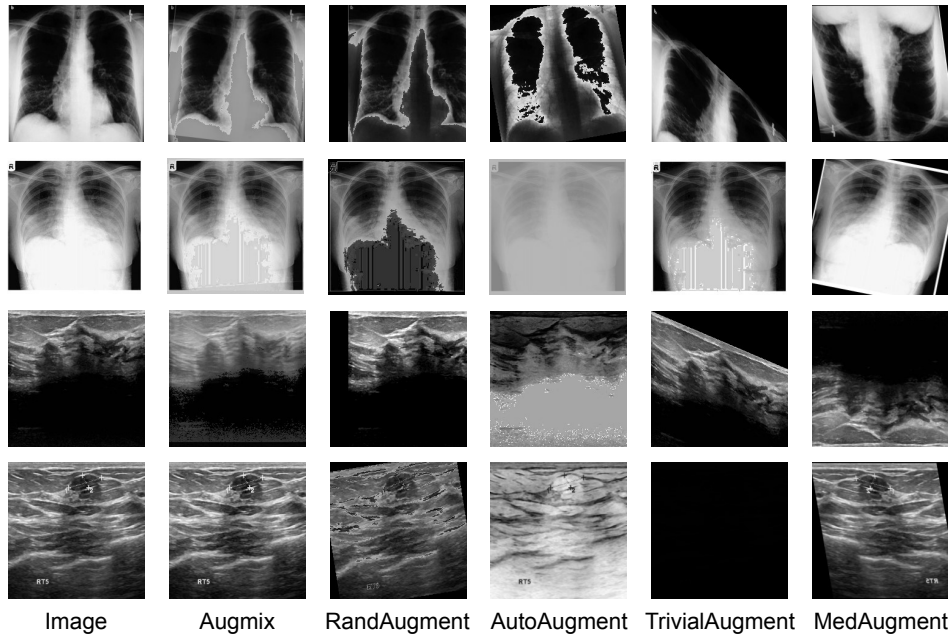


Figure 2: Examples of augmented medical images generated by different automatic DA methods.

3.2. Augmentation Spaces

We partite the DA operations into pixel-level and spatial-level DA operations and construct two augmentation spaces termed A_p and A_s with pixel-level and spatial-level DA operations respectively. To secure the eligibility of the proposed MedAugment for medical images, we exclude operations that can disrupt the details and features in medical images such as invert, equalize, and solarize. This results in the $A_p = \{\text{brightness, contrast, posterize, sharpness, gaussian blur, gaussian noise}\}$, and $A_s = \{\text{rotate, horizontal flip, vertical flip, scale, translate}_x, \text{translate}_y, \text{shear}_x, \text{shear}_y\}$. To prevent the operations in A_p from hampering the grey-level class information in the masks, we solely employ the operations from A_s for mask augmentation. To affirm compatibility and scalability, we leverage the well-established augmentation framework Albumentations [49] to perform conventional operations as it offers superior diversity [50–52].

3.3. Sampling Strategy

We present an effective sampling strategy II when sampling operations from A_p and A_s due to considerations from two aspects. Firstly, the medical images are sensitive to attributes such as `brightness`. Secondly, a large number of consecutive operations can lead to unrealistic output images that drift far from the original ones [44]. To this end, we regulate the maximum number of operations sampled from A_p and in total equals one and three, respectively. Besides, setting the total number of operations to one is considered inconsequential as it degrades to a single operation without combinations. Taking these factors into account, we affirm the number

of sequential operations $M = \{2, 3\}$. Given this setup, four sampling combinations $\Pi = \{\pi_1, \pi_2, \pi_3, \pi_4\}$ are produced, in which the number of the operations sampled from the two spaces equal $1 + 2$, $0 + 3$, $1 + 1$, and $0 + 2$, respectively. This number of combinations determines the number of the augment branches. For scalability consideration, we design the N in MedAugment extendable and alter the sampling to replacement sampling. Besides, the separate branch can be shielded. By setting $N = 1$ and shielding the separate branch, the MedAugment can be employed to perform one-to-one augmentation. In Figure 2, we compared the examples of augmented images generated by different methods. Through detailed observation, it can be found that MedAugment can produce the most realistic augmented images, preventing the breaking of the details and features in the medical images. The augmented images generated by the remaining approaches may be identifiable by the DL model but may lack clinical relevance or interpretability.

3.4. Hyperparameter Mapping

We propose a hyperparameter mapping relationship to produce a rational augmentation level and make the maximum magnitude M_A and probability P_A of each operation fully controllable using l . We observed that medical images are susceptible to the magnitude of several operations like `Posterize`. When the number of remaining bits decreases, the quality of the augmented images deteriorates substantially. Therefore, we meticulously design the magnitude for these types of operations based on extensive experiments to affirm the resultant augmented images retain their significance. We illustrate the mapping between l and M_A for different operations in Table 1. It is worth noting that operations without magnitude are indicated as $-$. For extendable consideration, the l can be set to $\{1, 2, 3, 4\}$ with higher values corresponding to greater augmentation. The function F returns an odd number based on the input l and is formulated as:

$$F(x) = \begin{cases} \lceil x \rceil + 1 & \lceil x \rceil = 2k \\ \lceil x \rceil & \lceil x \rceil = 2k + 1 \end{cases} \quad k \in \mathbb{Z} \quad (1)$$

where $\lceil \cdot \rceil$ represents round up. The probability for operations sampled from A_p and A_s adhere to the identical formulation, in which $P_A = 0.2l$.

4. Experiments and Results

4.1. Datasets

We leverage four datasets for classification performance evaluation. The breast ultrasound dataset (BUSI) [53] is collected from 600 female patients between 25 and 75 years old. It encompasses 780 images, of which 437, 210, and 133 images are benign, malignant, and normal, respectively. The average image resolution of BUSI is around 500×500 . The lung diseases X-ray dataset (LUNG) [54] is collected by researchers from Qatar University and the University of Dhaka. It consists of

Table 1: M_A for operations from A_p and A_s . $\lfloor \cdot \rfloor$ represents round down. The function F returns an integer odd number. Operations without magnitude are denoted as $-$.

Space	Operation	Magnitude	Parameter
A_p	Brightness	$0.04l$	Brightness
	Contrast	$0.04l$	Contrast
	Posterize	$\lfloor 8 - 0.8l \rfloor$	Number of bits left
	Sharpness	$(0.04l, 0.1l)$	Sharpened image visibility
	Gaussian blur	$(3, F(3 + 0.8l))$	Maximum Gaussian kernel size
	Gaussian noise	$(2l, 10l)$	Gaussian noise variance range
A_s	Rotate	$4l$	Rotation in degree
	Horizontal flip	$-$	Horizontal flip
	Vertical flip	$-$	Vertical flip
	Scale	$(1 - 0.04l, 1 + 0.04l)$	Scaling factor
	Translate_x	$(0, 2l)$	X translate in fraction
	Translate_y	$(0, 2l)$	Y translate in fraction
	Shear_x	$(0, 0.02l)$	X shear in degree
	Shear_y	$(0, 0.02l)$	Y shear in degree

three categories corresponding to COVID-19, severe acute respiratory syndrome, and Middle East Respiratory Syndrome and each category composes 423, 134, and 144 images, respectively. The brain tumor magnetic resonance imaging dataset (BTMRI) [55] is composed of four categories corresponding to glioma, meningioma, normal, and pituitary. Each category encompasses 1321, 1339, 1595, and 1457 images for training and 300, 306, 405, and 300 images for testing. The cataract eye camera dataset (CATAR) [56] consists of cataract and normal categories, in which 245 and 246 images are for training and 61 and 60 images are for testing.

We utilize three datasets for segmentation performance comparison including the LUNG, in which images and masks across different categories are merged. The endoscopic colonoscopy dataset (CVC) [57] serves as the official database leveraged in the training stages of the international conference on medical image computing and computer-assisted intervention and consists of 1224 polyp frames images and masks extracted from colonoscopy videos. The colonoscopy image dataset (Kvasir) [58] is composed of 1000 gastrointestinal polyp images and masks with a resolution varying from 332×487 to 1920×1072 .

4.2. Experimental Setup

We pre-process the data ahead of the model training. We divided the datasets into training, validation, and test subsets with a ratio of 6:2:2 or 8:2 in case the testing data are separately provided. For classification datasets, the proportion of each category in different subsets equals that of the original data. The class-balanced partition can prevent potential category imbalance. Images and masks are preprocessed to the resolution of 224×224 before executing augmentation and the augmentation is employed on the training subset solely. Following the one-to-five augmentation manner of MedAugment, the augmented training subset across all methods equals five times the size of the original training subset.

For classification, we leverage Adam as the optimizer with a decay factor of 0.01. We use cross-entropy as the loss function. The initial learning rate is 0.002 and decays step-wise for every 20 epochs with a factor of 0.9. The total epoch is 40 and the early stopping technique is employed with a patience of 8. The batch size is set as 128. We use VGGNet [59], ResNeXt [60] and ConvNeXt [61] for training. Models are evaluated based on metrics including accuracy (ACC), negative predictive value (NPV), positive predictive value (PPV), sensitivity (SEN), specificity (SPE), and F1 score (FOS). We compare our MedAugment with the SOTA GAN-based method StyleGAN2-ADA [62] and foundational and SOTA automatic DA methods including AutoAugment, AugMix, RandAugment, and TrivialAugment. Results reported are the mean across all categories when applicable.

Regarding segmentation, we utilize dice loss and the remaining hyperparameters follow the classification setup. For model training, we employ UNet++ [63], FPN [64], and DeepLabV3 [65], with ResNet-18 [66] serving as the encoder [67]. We evaluate the performance using dice score (DS), intersection over union (IoU), and pixel accuracy (PA). As mainstream SOTA automatic DA methods [34–36] are devised for classification, we propose conventional pipelines as SOTA approaches for performance comparison. Following the report [7] that horizontal flip, rotate, and vertical flip are the most prevalent implemented operations in the field of MIA, we present OneAugment, TwoAugment, and ThreeAugment. The OneAugment encompasses solely horizontal flip, while the TwoAugment and ThreeAugment are composed of successive horizontal flip, rotate and horizontal flip, rotate, vertical flip, respectively. The probability for each DA operation $p = 0.5$.

4.3. Classification Results

We demonstrate the classification results in Table 2, Table 3, and Table 4 for VGGNet, ResNeXt, and ConvNeXt, respectively. As can be observed, the proposed MedAugment overperforms SOTA methods across different models. Concerning VGGNet, MedAugment ranks first in 19 out of 24 metrics with 5 of them being joint. The highest accuracy of 83.4%, 85.1%, 89.3%, and 95.9% for the BUSI, LUNG, BTMRI, and CATAR datasets are achieved by the MedAugment. StyleGAN2-ADA shows superior performance on the BTMRI dataset and TrivialAugment achieves ideal results on the LUNG and CATAR datasets. For ResNeXt, MedAugment ranks first in 16 metrics with 3 being joint. The MedAugment achieves the highest accuracy of 79.0%, 85.8%, 87.2%, and 95.9% across the four datasets. StyleGAN2-ADA demonstrates leadership in the BUSI dataset and AugMix outperforms various methods in the CATAR dataset. Besides, the TrivialAugment achieves ideal results on the BUSI and LUNG datasets. Regarding ConvNeXt, MedAugment ranks first in 23 metrics and one exception is the PPV on the LUNG dataset. The highest accuracy of 78.3%, 85.8%, 86.3%, and 96.7% across different datasets are reached by MedAugment. It is worth noting that the CATAR dataset comprises few images in the test subset and thus may result in identical results. Moreover, relatively low SEN on BUSI, LUNG, and BTMRI datasets is observed, suggesting that the models can fail to correctly

Table 2: Classification results across different datasets using VGGNet. †: CATAR holds a small test subset and may result in identical performance. Results are reported in percentage and the best results are in bold.

Dataset	Metrics	StyleGAN2-ADA	AugMix	AutoAugment	RandAugment	TrivialAugment	MedAugment
BUSI	ACC	80.9	81.5	79.0	78.3	82.2	83.4
	NPV	89.6	89.7	88.5	87.8	90.3	91.8
	PPV	81.8	82.4	81.6	74.0	83.6	85.2
	SEN	76.4	75.9	71.8	74.4	75.8	76.6
	SPE	87.7	88.0	85.7	88.0	88.4	88.7
	FOS	77.9	78.3	75.3	74.1	78.4	79.8
LUNG	ACC	83.7	84.4	83.7	83.7	85.1	85.1
	NPV	91.1	92.1	90.9	91.0	93.1	92.0
	PPV	81.5	85.6	82.5	82.5	87.8	84.4
	SEN	77.5	77.1	78.4	77.6	76.5	78.8
	SPE	89.6	89.3	89.6	89.0	88.7	89.9
	FOS	79.0	79.8	79.5	79.5	80.7	81.0
BTMRI	ACC	89.3	89.0	86.1	87.3	87.6	89.3
	NPV	96.5	96.5	95.7	95.9	96.0	96.6
	PPV	88.9	89.2	86.0	87.4	87.5	90.0
	SEN	88.7	88.2	85.1	86.4	86.8	88.6
	SPE	96.4	96.3	95.3	95.7	95.8	96.4
	FOS	88.7	88.4	85.0	86.6	87.0	88.9
CATAR†	ACC	95.0	95.0	95.0	94.2	95.9	95.9
	NPV	95.1	95.1	95.0	94.2	96.0	95.9
	PPV	95.1	95.1	95.0	94.2	96.0	95.9
	SEN	95.1	95.1	95.0	94.2	95.9	95.9
	SPE	95.1	95.1	95.0	94.2	95.9	95.9
	FOS	95.0	95.0	95.0	94.2	95.9	95.9

classify true positive samples. This can be caused by the difficulty of identifying subtle abnormalities in medical images, especially when the abnormalities are in the early stage.

We visual the class activation map [68] across different automatic DA methods in Figure 3. We leverage the BUSI dataset as its tumor regions are markedly discernible against the background. This enables an intuitive differentiation of the overlay between the class activation map and the image. We employ VGGNet as it outperforms other models. Through observation, it can be found that the MedAugment enhances the ability of the model to accurately identify the correct regions. Although most approaches correctly concentrate the attention on the interested region, MedAugment achieves fuller coverage and fitter contouring. Compared to the alternatives, AutoAugment demonstrates suboptimal performance and the attention can lie on the incorrect region. We also illustrate an example in which the model cannot capture the tumor region regardless of the automatic DA method leveraged. This is plausible as the tumor region has trifling differences compared with the background and thus is difficult to capture.

We leverage t-SNE to visualize the performance across different DA methods on the BUSI dataset using VGGNet in Figure 4. We extract the features from the classi-

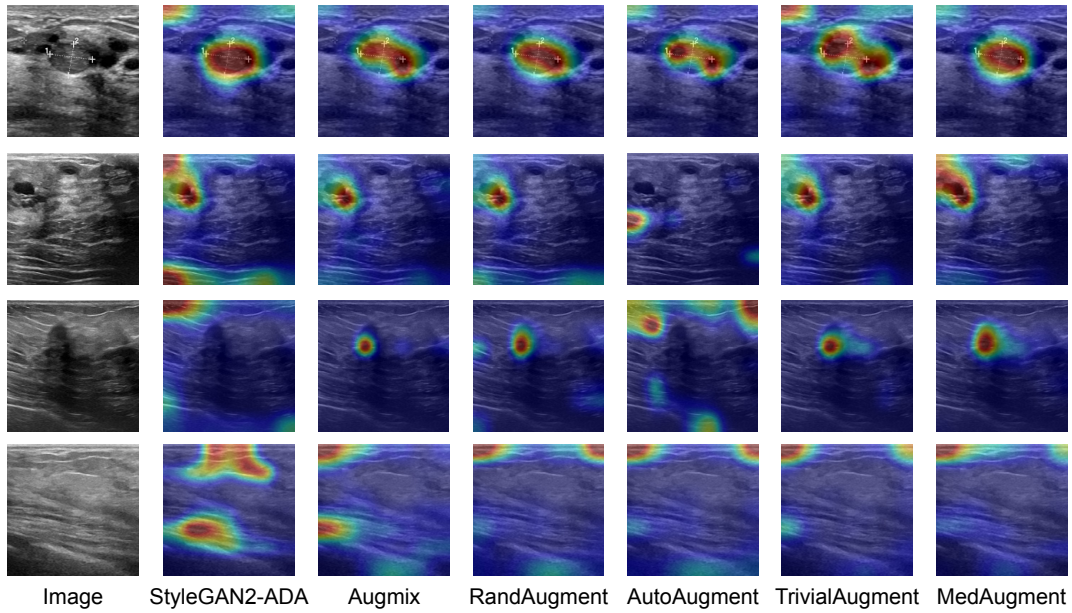


Figure 3: Comparison of the class activation map across different DA methods on the BUSI dataset using VGGNet.

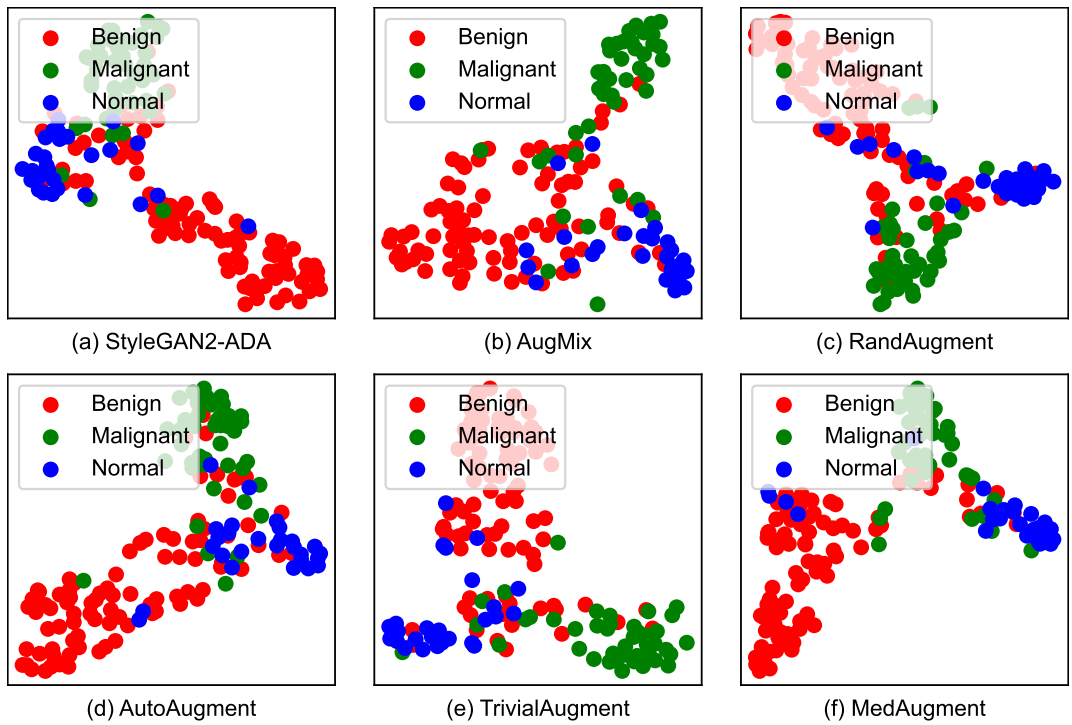


Figure 4: Comparison of t-SNE visualization across different DA methods on the BUSI dataset using VGGNet.

Table 3: Classification results across different datasets using ResNeXt.

Dataset	Metrics	StyleGAN2-ADA	AugMix	AutoAugment	RandAugment	TrivialAugment	MedAugment
BUSI	ACC	76.4	74.5	73.9	73.2	78.3	79.0
	NPV	87.3	85.2	85.3	84.9	87.5	88.8
	PPV	77.9	72.0	70.2	68.8	76.5	77.0
	SEN	68.2	71.8	73.9	68.0	76.2	72.7
	SPE	84.2	85.0	86.4	84.6	87.1	87.0
	FOS	71.5	71.8	71.6	68.4	76.2	74.4
LUNG	ACC	79.4	83.7	83.0	80.1	85.8	85.8
	NPV	88.9	92.0	92.2	90.5	93.4	92.6
	PPV	76.6	86.0	86.7	84.8	88.8	86.4
	SEN	71.3	75.0	73.1	69.1	77.8	79.4
	SPE	86.7	87.8	86.9	84.8	89.3	89.9
	FOS	72.9	79.0	77.7	73.7	81.8	82.3
BTMRI	ACC	85.2	86.0	86.3	84.4	86.4	87.2
	NPV	95.2	95.5	95.6	95.0	95.7	95.8
	PPV	84.6	85.6	85.6	83.9	86.0	86.7
	SEN	84.4	85.0	85.6	83.3	85.5	86.5
	SPE	95.1	95.3	95.5	94.7	95.4	95.8
	FOS	84.4	85.3	85.5	83.3	85.5	86.6
CATAR	ACC	95.0	95.9	95.0	95.0	95.0	95.9
	NPV	95.3	96.0	95.1	95.1	95.0	95.9
	PPV	95.3	96.0	95.1	95.1	95.0	95.9
	SEN	95.0	95.8	95.0	95.0	95.0	95.9
	SPE	95.0	95.8	95.0	95.0	95.0	95.9
	FOS	95.0	95.9	95.0	95.0	95.0	95.9

fication head behind the second linear layer and RELU activation function. Through detailed observation, it can be found that MedAugment achieves the closest point clusters within each category, especially for the malignant category. Moreover, the distance among different categories is longer compared with the remaining approaches. In comparison with the remaining methods, RandAugment performs relatively sub-optimal and the normal category overlaps with the benign and malignant categories to a large extent. Besides, AutoAugment does not preset distinct boundaries across varying categories. Intensive intra-class distribution coupled with sparse inter-class distribution can demonstrate the performance enhancement conferred by MedAugment.

4.4. Segmentation Results

We illustrate the segmentation results for UNet++, FPN, and DeepLabV3 in Table 5. It is observable that MedAugment reaches the highest performance compared with other methods. For UNet++, the MedAugment achieves the highest results for 8 of 9 metrics. The highest DS of 91.8%, 69.1%, and 68.1% on the LUNG, CVC, and Kvasir datasets are achieved by the MedAugment. The highest PA is secured by the OneAugment on the CVC dataset. Concerning the FPN, the MedAugment reaches the highest performance for 8 metrics with a joint. The highest DS of 94.7%, 77.3%, and 72.3% across the three datasets is realized by the MedAugment. TwoAugment

Table 4: Classification results across different datasets using ConvNeXt.

Dataset	Metrics	StyleGAN2-ADA	AugMix	AutoAugment	RandAugment	TrivialAugment	MedAugment
BUSI	ACC	77.1	76.4	77.1	76.4	77.1	78.3
	NPV	88.3	87.7	87.6	87.4	87.7	88.9
	PPV	77.6	76.9	75.7	76.8	78.0	79.5
	SEN	67.3	68.7	69.9	68.2	70.3	70.7
	SPE	84.7	84.5	85.4	84.4	85.0	85.5
	FOS	70.5	71.2	72.0	71.2	72.5	73.6
LUNG	ACC	82.3	83.7	82.3	81.6	85.1	85.8
	NPV	91.4	91.6	91.4	91.6	92.6	93.0
	PPV	86.2	85.8	85.0	87.2	87.9	87.2
	SEN	72.8	76.1	72.6	70.6	77.5	78.8
	SPE	86.3	87.8	86.6	85.4	88.7	89.6
	FOS	77.3	79.6	76.9	75.8	81.4	82.0
BTMRI	ACC	85.7	85.7	85.3	84.7	85.6	86.3
	NPV	95.4	95.5	95.3	95.2	95.4	95.6
	PPV	85.3	85.5	84.8	84.1	85.2	86.4
	SEN	85.2	84.8	84.6	83.9	84.8	85.6
	SPE	95.3	95.2	95.1	94.9	95.2	95.4
	FOS	85.0	84.7	84.3	83.5	84.7	85.6
CATAR	ACC	95.0	95.9	95.0	95.0	94.2	96.7
	NPV	95.1	95.9	95.0	95.0	94.3	96.7
	PPV	95.1	95.9	95.0	95.0	94.3	96.7
	SEN	95.1	95.9	95.0	95.0	94.2	96.7
	SPE	95.1	95.9	95.0	95.0	94.2	96.7
	FOS	95.0	95.9	95.0	95.0	94.2	96.7

demonstrates superior performance on the CVC dataset. Regarding DeepLabV3, the MedAugment achieves the highest performance across all metrics with a joint. The highest DS of 93.3%, 80.0%, and 72.3% across different datasets is realized by the MedAugment. The TwoAugment achieves the identical PA on the Kvasir dataset. It is worth noting that we observed significantly high PA compared with DS and IoU. Though a high PA may indicate superior model performance, the predicted pixels may be dispersed and thus not considered ideal.

We present the comparison of predicted and ground truth masks across different methods in Figure 5. We leverage the LUNG dataset as its lung object holds regular-shaped morphology and thus facilitates the clear discernment of subtle differences across varying methods. We employ FPN according to its superior performance. Through detailed observations, we can find that the model trained with MedAugment can produce the most accurate masks compared with the ground truth, and the performance improvement can be reflected from two aspects. Firstly, it reduces the number of pixels to be incorrectly predicted. Secondly, it improves the ability of the model to predict smoother edge curves and more accurate contours. Comparing with the remaining approaches, it can be found that the ThreeAugment and OneAugment can produce irregular bulges and the TwoAugment and ThreeAugment approaches predict jagged and unregular contours.

We compare the Bland-Altman plot across different DA methods on the LUNG

Table 5: Segmentation results across different datasets using various models.

Model	Dataset	Metrics	OneAugment	TwoAugment	ThreeAugment	MedAugment
UNet++	LUNG	DS	86.5	89.5	89.5	91.8
		IoU	77.0	82.0	82.5	85.8
		PA	93.2	95.1	95.2	96.1
	CVC	DS	63.1	65.9	62.2	69.1
		IoU	54.8	55.3	51.9	58.1
		PA	95.2	93.7	93.4	93.9
	Kvasir	DS	63.4	67.3	66.1	68.1
		IoU	51.3	55.7	54.9	56.8
		PA	85.4	90.9	90.2	91.2
FPN	LUNG	DS	94.1	90.4	85.5	94.7
		IoU	89.1	83.3	76.7	90.1
		PA	96.9	95.2	93.0	97.2
	CVC	DS	72.5	76.3	74.3	77.3
		IoU	62.2	66.8	63.4	66.8
		PA	94.6	95.4	94.8	94.7
	Kvasir	DS	67.4	66.2	66.2	72.3
		IoU	56.4	55.1	53.6	61.6
		PA	91.0	90.7	88.0	91.3
DeepLabV3	LUNG	DS	84.7	91.3	92.0	93.3
		IoU	74.5	84.5	85.6	87.7
		PA	92.7	95.6	96.0	96.6
	CVC	DS	77.9	77.0	77.2	80.0
		IoU	67.3	68.0	67.2	70.9
		PA	95.0	95.9	95.4	96.2
	Kvasir	DS	70.4	69.0	63.8	72.3
		IoU	60.2	57.8	52.6	61.4
		PA	91.0	92.1	90.6	92.1

dataset using FPN to illustrate the relationship between the predicted and the ground truth mask for each test image in Fig. 6. We count the number of the object pixels in the predicted masks, divide the results by the number of total pixels, and compare the output with that of the ground truth masks. From the results, it can be found that the MedAugment achieves the lowest mean and standard deviation of 0.19% and 1.96%, respectively. In comparison with SOTA methods, the ThreeAugment demonstrates relatively suboptimal performance with a mean and standard deviation of 4.53% and 6.87%, respectively. Moreover, most of the data points are located within the 95% limits of agreement, demonstrating the superior consistency across the predicted and ground truth masks. Furthermore, the data do not show a consistent trend difference, indicating the absence of significant systematic discrepancies.

4.5. Ablation Study

We design an ablation approach with one augmentation space and random sampling to validate the effectiveness of the proposed augmentation spaces and sampling strategy. Under this setup, the augmentation space consists of fourteen operations and $M = \{2, 3\}$ operations are randomly sampled each time. We lever-

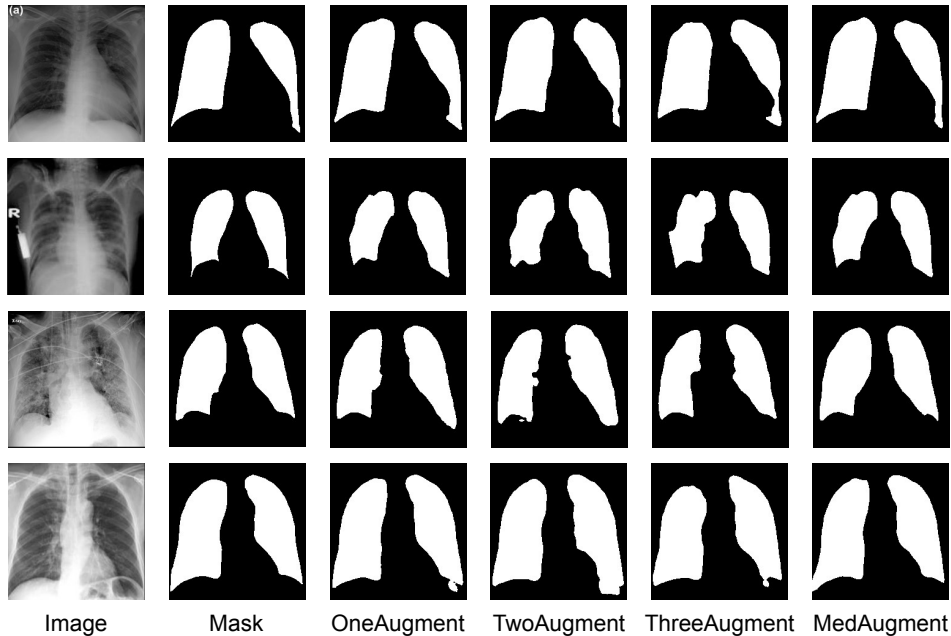


Figure 5: Comparison of predicted and ground truth masks across different DA methods on the LUNG dataset using FPN.

age the LUNG dataset as employing the consistent dataset across classification and segmentation tasks can produce more convincing results. We demonstrate the performance comparison between the ablation approach and MedAugment setups on the LUNG dataset in Figure 7 and Figure 8, for classification and segmentation tasks respectively. In the context of classification, it is observable that a majority of the metrics exhibit a decreasing trend, with only a few metrics demonstrating an increase. Furthermore, the extent of the decrease is more pronounced compared with the increase. Regarding segmentation, we observed that all the metrics decreased with a higher magnitude compared with classification. This observation aligns with our expectations as random sampling within the pixel augmentation space A_p may yield unrealistic augmented images exemplified in Figure 2, albeit to a lesser extent than those generated by the abovementioned methods. Additionally, pixel-level segmentation is more vulnerable to unrealistic images.

We investigate the impact of the augmentation level by validating the performance of MedAugment under $l = \{1, 2, 3, 4\}$. We compare the performance across different l on the LUNG dataset in Figure 9 and Figure 10, for classification and segmentation tasks respectively. Concerning classification, it can be found that the model performance does not present dramatic fluctuation as the varying of l . Although $l = 5$ demonstrates performance leadership in most cases, a portion of metrics such as the SEN in ConvNeXt can be relatively low. In the context of segmentation, the $l = 5$ achieves higher performance leadership compared with the remaining values, and the highest ACC, NPV, and PPV are secured simultaneously.

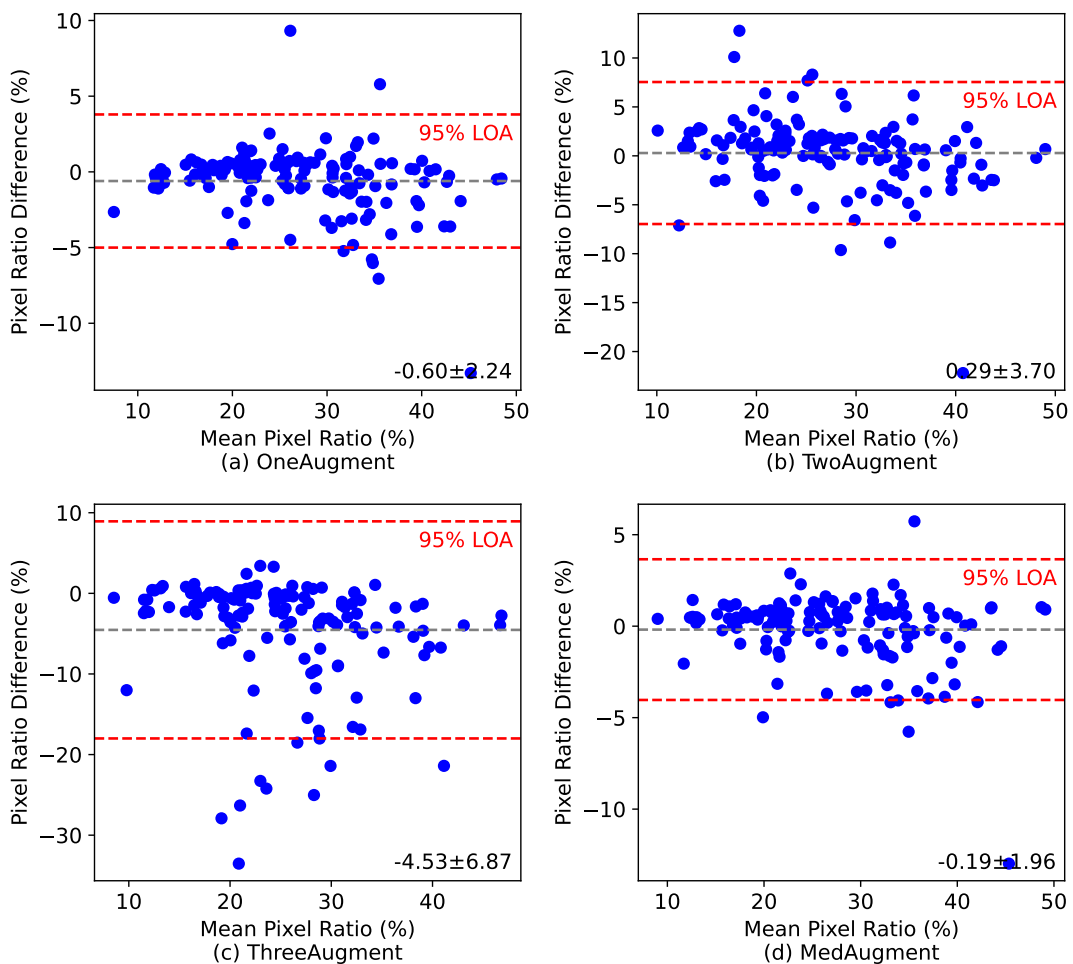


Figure 6: Comparison of Bland-Altman plot across different DA methods on the LUNG dataset using FPN.

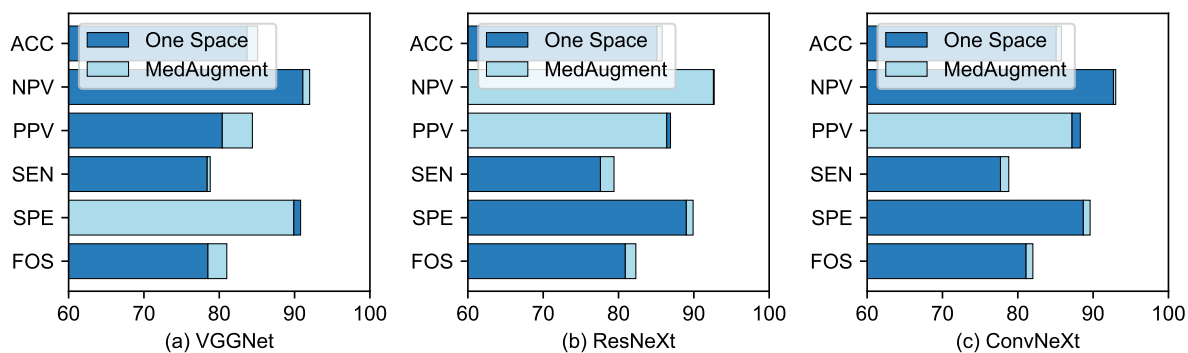


Figure 7: Comparison of classification results between leveraging one augmentation space and MedAugment on the LUNG dataset.

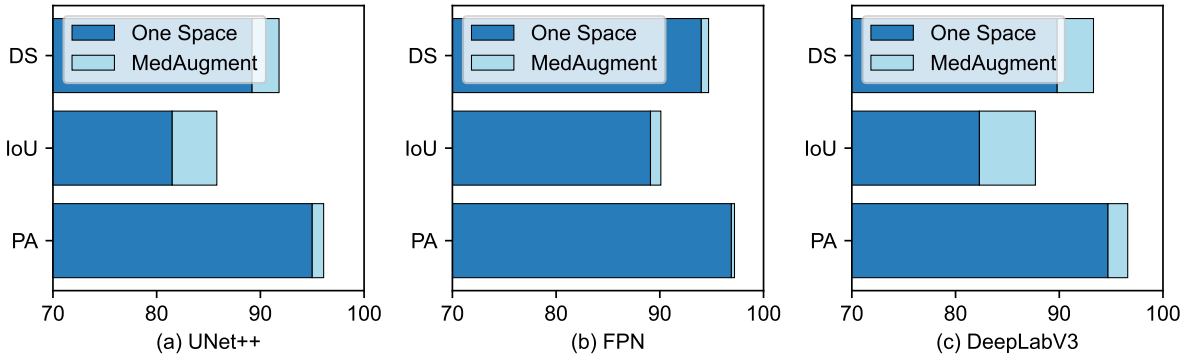


Figure 8: Comparison of segmentation results between leveraging one augmentation space and MedAugment on the LUNG dataset.

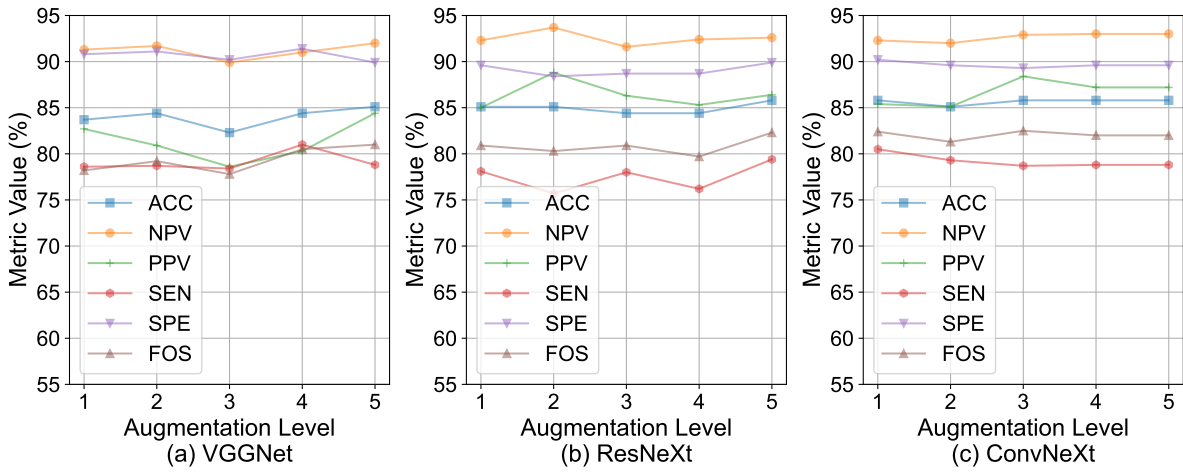


Figure 9: Comparison of classification metrics across different l on the LUNG dataset.

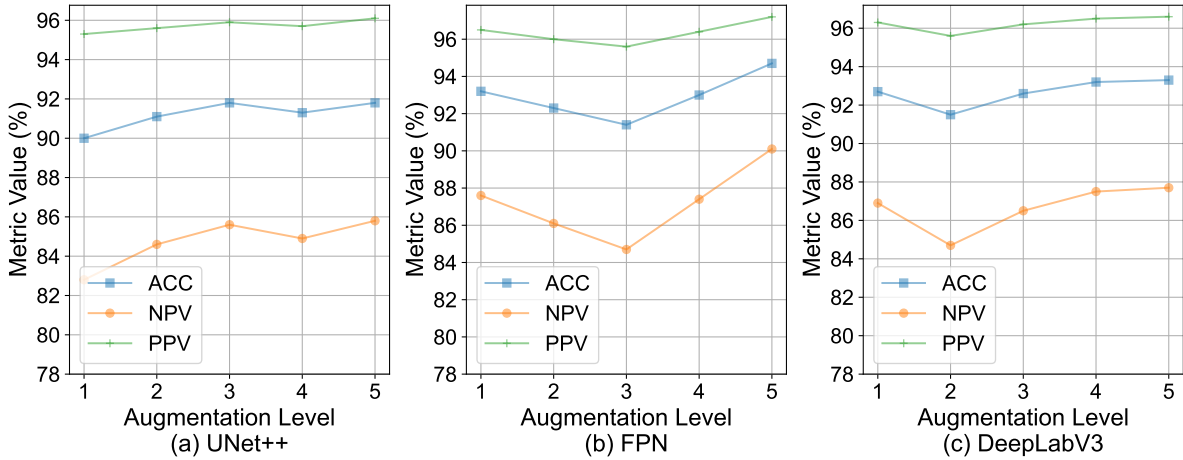


Figure 10: Comparison of segmentation metrics across different l on the LUNG dataset.

5. Conclusions

In this paper, we propose an efficient and effective automatic DA method termed MedAugment. We develop the pixel augmentation space and spatial augmentation space and exclude the operations that can disrupt the details and features within medical images. Besides, we propose a sampling strategy by constraining the number of operations sampled from the proposed spaces. Furthermore, we formulate a hyperparameter mapping relationship to produce a rational augmentation level and secure the proposed approach fully controllable with a single hyperparameter. These revisions can address the differences between natural and medical images. Extensive experimental results on seven public medical datasets demonstrate the effectiveness of the presented MedAugment. We believe that the plug-and-use and training-free MedAugment may benefit the MIA community, especially the medical experts without solid DL foundations. Despite its superior performance, several challenges arise. Firstly, an effective metric balancing approach can be necessary as the performance gap across different metrics is high and several metrics such as SEN do not present ideal results. Specifically, varying hyperparameters can be employed to balance different metrics through hyperparameter updating during training. Secondly, the challenge of dealing with small object sizes requires further investigation to reduce the likelihood of mistaken categorization to the background. This leads to the way of emphasizing small objects, such as leveraging varying types and levels of operations according to the size of the object. Distinctly, images with smaller objects may have a higher probability of being scaled with a larger factor during augmentation compared to those with larger objects.

References

- [1] Ziduo Yang, Lu Zhao, Shuyu Wu, and Calvin Yu-Chian Chen. Lung lesion localization of covid-19 from chest ct image: A novel weakly supervised learning method. *IEEE J. Biomed. Health Inform.*, 25(6):1864–1872, 2021. <https://doi.org/10.1109/JBHI.2021.3067465>.
- [2] S Poonkodi and M Kanchana. 3d-medtrancsgan: 3d medical image transformation using csgan. *Comput. Biol. Med.*, page 106541, 2023. <https://doi.org/10.1016/j.combiomed.2023.106541>.
- [3] Jialei Chen, Chong Fu, Haoyu Xie, Xu Zheng, Rong Geng, and Chiu-Wing Sham. Uncertainty teacher with dense focal loss for semi-supervised medical image segmentation. *Comput. Biol. Med.*, 149:106034, 2022. <https://doi.org/10.1016/j.combiomed.2022.106034>.
- [4] Jun Li, Junyu Chen, Yucheng Tang, Ce Wang, Bennett A Landman, and S Kevin Zhou. Transforming medical imaging with transformers? a comparative review of key properties, current progresses, and future perspectives. *Med. Image Anal.*, page 102762, 2023. <https://doi.org/10.1016/j.media.2023.102762>.

- [5] Jia Deng, Wei Dong, Richard Socher, Li-Jia Li, Kai Li, and Li Fei-Fei. Imagenet: A large-scale hierarchical image database. In *Proceedings of the IEEE conference on computer vision and pattern recognition*, pages 248–255. Ieee, 2009.
- [6] Zhaoshan Liu, Qiujie Lv, Chau Hung Lee, and Lei Shen. Gsda: Generative adversarial network-based semi-supervised data augmentation for ultrasound image classification. *Heliyon*, 9(9), 2023.
- [7] Matthias Eisenmann, Annika Reinke, Vivienn Weru, Minu Dietlinde Tizabi, Fabian Isensee, Tim J Adler, Sharib Ali, Vincent Andrearczyk, Marc Aubreville, Ujjwal Baid, et al. Why is the winner the best? *arXiv preprint*, 2023. <https://doi.org/10.48550/arXiv.2303.17719>.
- [8] Tiantian Fang. A novel computer-aided lung cancer detection method based on transfer learning from googlenet and median intensity projections. In *Proceedings of the IEEE international conference on computer and communication engineering technology*, pages 286–290. IEEE, 2018. <https://doi.org/10.1109/CCET.2018.8542189>.
- [9] Christina Gsaxner, Peter M Roth, Jürgen Wallner, and Jan Egger. Exploit fully automatic low-level segmented pet data for training high-level deep learning algorithms for the corresponding ct data. *PloS one*, 14(3):e0212550, 2019. <https://doi.org/10.1371/journal.pone.0212550>.
- [10] Mahendra Khened, Varghese Alex Kollerathu, and Ganapathy Krishnamurthi. Fully convolutional multi-scale residual densenets for cardiac segmentation and automated cardiac diagnosis using ensemble of classifiers. *Medical image analysis*, 51:21–45, 2019. <https://doi.org/10.1016/j.media.2018.10.004>.
- [11] Harshit Kaushik, Dilbag Singh, Manjit Kaur, Hammam Alshazly, Atef Zaguia, and Habib Hamam. Diabetic retinopathy diagnosis from fundus images using stacked generalization of deep models. *IEEE Access*, 9:108276–108292, 2021.
- [12] Fabian Isensee, Paul F Jaeger, Simon AA Kohl, Jens Petersen, and Klaus H Maier-Hein. nnu-net: a self-configuring method for deep learning-based biomedical image segmentation. *Nature methods*, 18(2):203–211, 2021.
- [13] Ian Goodfellow, Jean Pouget-Abadie, Mehdi Mirza, Bing Xu, David Warde-Farley, Sherjil Ozair, Aaron Courville, and Yoshua Bengio. Generative adversarial nets. *Advances in neural information processing systems*, 27, 2014.
- [14] Lu Chai, Zidong Wang, Jianqing Chen, Guokai Zhang, Fawaz E Alsaadi, Fuad E Alsaadi, and Qinyuan Liu. Synthetic augmentation for semantic segmentation of class imbalanced biomedical images: A data pair generative adversarial network approach. *Computers in Biology and Medicine*, 150:105985, 2022.

- [15] Daiqing Li, Junlin Yang, Karsten Kreis, Antonio Torralba, and Sanja Fidler. Semantic segmentation with generative models: Semi-supervised learning and strong out-of-domain generalization. In *Proceedings of the IEEE/CVF Conference on Computer Vision and Pattern Recognition*, pages 8300–8311, 2021.
- [16] Jason Kugelman, David Alonso-Caneiro, Scott A Read, Stephen J Vincent, Fred K Chen, and Michael J Collins. Dual image and mask synthesis with gans for semantic segmentation in optical coherence tomography. In *2020 Digital Image Computing: Techniques and Applications (DICTA)*, pages 1–8. IEEE, 2020.
- [17] Siddharth Pandey, Pranshu Ranjan Singh, and Jing Tian. An image augmentation approach using two-stage generative adversarial network for nuclei image segmentation. *Biomedical Signal Processing and Control*, 57:101782, 2020.
- [18] Ahmed Iqbal and Muhammad Sharif. Unet: A semi-supervised method for segmentation of breast tumor images using a u-shaped pyramid-dilated network. *Expert Systems with Applications*, 221:119718, 2023.
- [19] Ali Madani, Mehdi Moradi, Alexandros Karargyris, and Tanveer Syeda-Mahmood. Semi-supervised learning with generative adversarial networks for chest x-ray classification with ability of data domain adaptation. In *Proceedings of the IEEE International Symposium on Biomedical Imaging*, pages 1038–1042, 2018. <https://doi.org/10.1109/ISBI.2018.8363749>.
- [20] Ting Pang, Jeannie Hsiu Ding Wong, Wei Lin Ng, and Chee Seng Chan. Semi-supervised gan-based radiomics model for data augmentation in breast ultrasound mass classification. *Comput. Meth. Programs Biomed.*, 203:106018, 2021. <https://doi.org/10.1016/j.cmpb.2021.106018>.
- [21] Maayan Frid-Adar, Idit Diamant, Eyal Klang, Michal Amitai, Jacob Goldberger, and Hayit Greenspan. Gan-based synthetic medical image augmentation for increased cnn performance in liver lesion classification. *Neurocomputing*, 321:321–331, 2018. <https://doi.org/10.1016/j.neucom.2018.09.013>.
- [22] Andrew Beers, James Brown, Ken Chang, J Peter Campbell, Susan Ostmo, Michael F Chiang, and Jayashree Kalpathy-Cramer. High-resolution medical image synthesis using progressively grown generative adversarial networks. *arXiv preprint arXiv:1805.03144*, 2018.
- [23] Francesco Calimeri, Aldo Marzullo, Claudio Stamile, and Giorgio Terracina. Biomedical data augmentation using generative adversarial neural networks. In *International conference on artificial neural networks*, pages 626–634. Springer, 2017.

- [24] Qianli Feng, Chenqi Guo, Fabian Benitez-Quiroz, and Aleix M Martinez. When do gans replicate? on the choice of dataset size. In *Proceedings of the IEEE/CVF International Conference on Computer Vision*, pages 6701–6710, 2021.
- [25] Tero Karras, Samuli Laine, and Timo Aila. A style-based generator architecture for generative adversarial networks. In *Proceedings of the IEEE/CVF conference on computer vision and pattern recognition*, pages 4401–4410, 2019.
- [26] Jonathan Ho, Ajay Jain, and Pieter Abbeel. Denoising diffusion probabilistic models. *Advances in neural information processing systems*, 33:6840–6851, 2020.
- [27] Puria Azadi Moghadam, Sanne Van Dalen, Karina C Martin, Jochen Lennerz, Stephen Yip, Hossein Farahani, and Ali Bashashati. A morphology focused diffusion probabilistic model for synthesis of histopathology images. In *Proceedings of the IEEE/CVF Winter Conference on Applications of Computer Vision*, pages 2000–2009, 2023.
- [28] Walter HL Pinaya, Petru-Daniel Tudosiu, Jessica Dafflon, Pedro F Da Costa, Virginia Fernandez, Parashkev Nachev, Sebastien Ourselin, and M Jorge Cardoso. Brain imaging generation with latent diffusion models. In *MICCAI Workshop on Deep Generative Models*, pages 117–126. Springer, 2022.
- [29] Firas Khader, Gustav Müller-Franzes, Soroosh Tayebi Arasteh, Tianyu Han, Christoph Haarbuerger, Maximilian Schulze-Hagen, Philipp Schad, Sandy Engelhardt, Bettina Baeßler, Sebastian Foersch, et al. Denoising diffusion probabilistic models for 3d medical image generation. *Scientific Reports*, 13(1):7303, 2023.
- [30] Fenghe Tang, Jianrui Ding, Lingtao Wang, Min Xian, and Chunping Ning. Multi-level global context cross consistency model for semi-supervised ultrasound image segmentation with diffusion model. *arXiv preprint arXiv:2305.09447*, 2023.
- [31] Ekin D Cubuk, Barret Zoph, Dandelion Mane, Vijay Vasudevan, and Quoc V Le. Autoaugment: Learning augmentation strategies from data. In *Proceedings of the IEEE/CVF conference on computer vision and pattern recognition*, pages 113–123, 2019.
- [32] Sungbin Lim, Ildoo Kim, Taesup Kim, Chiheon Kim, and Sungwoong Kim. Fast autoaugment. *Advances in Neural Information Processing Systems*, 32, 2019.
- [33] Daniel Ho, Eric Liang, Xi Chen, Ion Stoica, and Pieter Abbeel. Population based augmentation: Efficient learning of augmentation policy schedules. In *International Conference on Machine Learning*, pages 2731–2741. PMLR, 2019.

- [34] Ekin D Cubuk, Barret Zoph, Jonathon Shlens, and Quoc V Le. Randaugment: Practical automated data augmentation with a reduced search space. In *Proceedings of the IEEE/CVF conference on computer vision and pattern recognition workshops*, pages 702–703, 2020.
- [35] Samuel G Müller and Frank Hutter. Trivialaugument: Tuning-free yet state-of-the-art data augmentation. In *Proceedings of the IEEE/CVF international conference on computer vision*, pages 774–782, 2021.
- [36] Tom Ching LingChen, Ava Khonsari, Amirreza Lashkari, Mina Rafi Nazari, Jaspreet Singh Sambee, and Mario A Nascimento. Uniformaugument: A search-free probabilistic data augmentation approach. *arXiv preprint*, 2020. <https://doi.org/10.48550/arXiv.2003.14348>.
- [37] Tiexin Qin, Ziyuan Wang, Kelei He, Yinghuan Shi, Yang Gao, and Dinggang Shen. Automatic data augmentation via deep reinforcement learning for effective kidney tumor segmentation. In *ICASSP 2020-2020 IEEE International Conference on Acoustics, Speech and Signal Processing (ICASSP)*, pages 1419–1423. IEEE, 2020.
- [38] Ju Xu, Mengzhang Li, and Zhanxing Zhu. Automatic data augmentation for 3d medical image segmentation. In *Medical Image Computing and Computer Assisted Intervention–MICCAI 2020: 23rd International Conference, Lima, Peru, October 4–8, 2020, Proceedings, Part I 23*, pages 378–387. Springer, 2020.
- [39] Junyan Lyu, Yiqi Zhang, Yijin Huang, Li Lin, Pujin Cheng, and Xiaoying Tang. Aadg: automatic augmentation for domain generalization on retinal image segmentation. *IEEE Transactions on Medical Imaging*, 41(12):3699–3711, 2022.
- [40] Dong Yang, Holger Roth, Ziyue Xu, Fausto Milletari, Ling Zhang, and Daguang Xu. Searching learning strategy with reinforcement learning for 3d medical image segmentation. In *Medical Image Computing and Computer Assisted Intervention–MICCAI 2019: 22nd International Conference, Shenzhen, China, October 13–17, 2019, Proceedings, Part II 22*, pages 3–11. Springer, 2019.
- [41] Zhaoshan Liu, Qiujie Lv, Ziduo Yang, Yifan Li, Chau Hung Lee, and Lei Shen. Recent progress in transformer-based medical image analysis. *arXiv preprint*, 2022. <https://doi.org/10.48550/arXiv.2208.06643>.
- [42] Cheng Ouyang, Carlo Biffi, Chen Chen, Turkey Kart, Huaqi Qiu, and Daniel Rueckert. Self-supervised learning for few-shot medical image segmentation. *IEEE Trans. Med. Imaging*, 41(7):1837–1848, 2022. <https://doi.org/10.1109/TMI.2022.3150682>.
- [43] Toan Tran, Trung Pham, Gustavo Carneiro, Lyle Palmer, and Ian Reid. A bayesian data augmentation approach for learning deep models. *Advances in neural information processing systems*, 30, 2017.

- [44] Dan Hendrycks, Norman Mu, Ekin D Cubuk, Barret Zoph, Justin Gilmer, and Balaji Lakshminarayanan. Augmix: A simple data processing method to improve robustness and uncertainty. *arXiv preprint*, 2019. <https://doi.org/10.48550/arXiv.1912.02781>.
- [45] Tero Karras, Timo Aila, Samuli Laine, and Jaakko Lehtinen. Progressive growing of gans for improved quality, stability, and variation. *arXiv preprint arXiv:1710.10196*, 2017.
- [46] Emily L Denton, Soumith Chintala, Rob Fergus, et al. Deep generative image models using a laplacian pyramid of adversarial networks. *Advances in neural information processing systems*, 28, 2015.
- [47] Robin Rombach, Andreas Blattmann, Dominik Lorenz, Patrick Esser, and Björn Ommer. High-resolution image synthesis with latent diffusion models. In *Proceedings of the IEEE/CVF conference on computer vision and pattern recognition*, pages 10684–10695, 2022.
- [48] Ziyu Wang, Tom Schaul, Matteo Hessel, Hado Hasselt, Marc Lanctot, and Nando Freitas. Dueling network architectures for deep reinforcement learning. In *International conference on machine learning*, pages 1995–2003. PMLR, 2016.
- [49] Alexander Buslaev, Vladimir I Iglovikov, Eugene Khvedchenya, Alex Parinov, Mikhail Druzhinin, and Alexandr A Kalinin. Alumentations: fast and flexible image augmentations. *Information*, 11(2):125, 2020. <https://doi.org/10.3390/info11020125>.
- [50] Adam Paszke, Sam Gross, Francisco Massa, Adam Lerer, James Bradbury, Gregory Chanan, Trevor Killeen, Zeming Lin, Natalia Gimelshein, Luca Antiga, et al. Pytorch: An imperative style, high-performance deep learning library. *Advances in neural information processing systems*, 32, 2019.
- [51] Fernando Pérez-García, Rachel Sparks, and Sébastien Ourselin. Torchio: a python library for efficient loading, preprocessing, augmentation and patch-based sampling of medical images in deep learning. *Computer Methods and Programs in Biomedicine*, 208:106236, 2021.
- [52] Isensee Fabian, Jäger Paul, Wasserthal Jakob, Zimmerer David, Petersen Jens, Kohl Simon, Schock Justus, Klein Andre, Roß Tobias, Wirkert Sebastian, et al. Batchgenerators—a python framework for data augmentation. *Division Med. Image Computing German Cancer Res. Center, Appl. Comput. Vis. Lab, Hamburg, Germany, Tech. Rep*, 2020.
- [53] Walid Al-Dhabyani, Mohammed Gomaa, Hussien Khaled, and Aly Fahmy. Dataset of breast ultrasound images. *Data in brief*, 28:104863, 2020. <https://doi.org/10.1016/j.dib.2019.104863>.

- [54] Anas M Tahir, Yazan Qiblawey, Amith Khandakar, Tawsifur Rahman, Uzair Khurshid, Farayi Musharavati, MT Islam, Serkan Kiranyaz, Somaya Al-Maadeed, and Muhammad EH Chowdhury. Deep learning for reliable classification of covid-19, mers, and sars from chest x-ray images. *Cognitive Computation*, pages 1–21, 2022. <https://doi.org/10.1007/s12559-021-09955-1>.
- [55] Brain tumor mri dataset. <https://www.kaggle.com/datasets/masoudnickparvar/brain-tumor-mri-dataset>. Accessed 26 April 2023.
- [56] Cataract dataset. <https://www.kaggle.com/datasets/nandanp6/cataract-image-dataset>. Accessed 26 April 2023.
- [57] Cvc-clinicdb. <https://www.kaggle.com/datasets/balraj98/cvcclinicdb>. Accessed 3 May 2023.
- [58] Kvasir seg. <https://datasets.simula.no/kvasir-seg/>. Accessed 3 May 2023.
- [59] Karen Simonyan and Andrew Zisserman. Very deep convolutional networks for large-scale image recognition. *arXiv preprint arXiv:1409.1556*, 2014.
- [60] Saining Xie, Ross Girshick, Piotr Dollár, Zhuowen Tu, and Kaiming He. Aggregated residual transformations for deep neural networks. In *Proceedings of the IEEE conference on computer vision and pattern recognition*, pages 1492–1500, 2017.
- [61] Zhuang Liu, Hanzi Mao, Chao-Yuan Wu, Christoph Feichtenhofer, Trevor Darrell, and Saining Xie. A convnet for the 2020s. In *Proceedings of the IEEE/CVF Conference on Computer Vision and Pattern Recognition*, pages 11976–11986, 2022.
- [62] Tero Karras, Miika Aittala, Janne Hellsten, Samuli Laine, Jaakko Lehtinen, and Timo Aila. Training generative adversarial networks with limited data. *Advances in neural information processing systems*, 33:12104–12114, 2020.
- [63] Zongwei Zhou, Md Mahfuzur Rahman Siddiquee, Nima Tajbakhsh, and Jianming Liang. Unet++: A nested u-net architecture for medical image segmentation. In *Proceedings of the Deep Learning in Medical Image Analysis and Multimodal Learning for Clinical Decision Support*, pages 3–11. Springer, 2018.
- [64] Tsung-Yi Lin, Piotr Dollár, Ross Girshick, Kaiming He, Bharath Hariharan, and Serge Belongie. Feature pyramid networks for object detection. In *Proceedings of the IEEE conference on computer vision and pattern recognition*, pages 2117–2125, 2017.

- [65] Liang-Chieh Chen, George Papandreou, Florian Schroff, and Hartwig Adam. Rethinking atrous convolution for semantic image segmentation. *arXiv preprint arXiv:1706.05587*, 2017.
- [66] Kaiming He, Xiangyu Zhang, Shaoqing Ren, and Jian Sun. Deep residual learning for image recognition. In *Proceedings of the IEEE conference on computer vision and pattern recognition*, pages 770–778, 2016.
- [67] Pavel Iakubovskii. Segmentation models pytorch. https://github.com/qubvel/segmentation_models.pytorch, 2019. Accessed 3 May 2023.
- [68] François-Guillaume Fernandez. Torchcam: class activation explorer. <https://github.com/frgfm/torch-cam>, 2020. Accessed 6 May 2023.